UAV-based mapping, back analysis and trajectory modelling of a co-seismic rockfall in Lefkada Island, Greece

Charalampos Saroglou[1*],

Pavlos Asteriou[1]

Dimitrios Zekkos[2]

George Tsiambaos[1]

Marin Clark[3]

John Manousakis[4]

[1]Department of Geotechnical Engineering, School of Civil Engineering, National Technical University of Athens

[2]Department of Civil and Environmental Engineering, University of Michigan, USA

[3]Department of Earth and Environmental Science, University of Michigan, USA

[4]Elxis Group, S.A, Athens, Greece

* corresponding author: saroglou@central.ntua.gr

Abstract

We present field evidence and a kinematic study of rock block motion mobilised in the Ponti area by a M_w 6.5 earthquake near the island of Lefkada on 17th November 2015. A detailed survey was conducted using an Unmanned Aerial Vehicle (UAV) with an ultra-high definition (UHD) camera, which produced a high-resolution orthophoto and a Digital Terrain Model (DTM). The sequence of impact marks from the rock trajectory on the ground surface was identified from the orthophoto and field verified. Earthquake characteristics were used to estimate the acceleration of the rock slope and the initial condition of the detached block. Using the impact points from the measured rockfall trajectory, an analytical reconstruction of the trajectory was undertaken, which led to insights on the coefficients of restitution. The measured trajectory was compared with modeled rockfall trajectories using recommended

parameters. However, the actual trajectory could not be accurately predicted, revealing limitations of existing rockfall analysis software used in engineering practice.

Keywords

Rockfall, earthquake, DSM, DTM, modelling, restitution, UAV

1. Introduction

Active faulting, rock fracturing and high rates of seismicity contribute to a high rockfall hazard in Greece. Rockfalls primarily damage roadways and houses (Saroglou, 2013) and are most often triggered by rainfall and, secondly, seismic loading. In recent years, some rockfalls have impacted archaeological sites (Marinos & Tsiambaos, 2002, Saroglou et al., 2012). The Ionian Islands, which include Lefkada Island, experience frequent M_w 5-6.5 earthquakes, as well as less frequent larger (up to 7.5) earthquakes. The historical seismological record for the island is particularly well constrained with reliable detailed information for at least 23 such earthquake events that induced ground failure since 1612. On average, Lefkada experiences a damaging earthquake every 18 years. In the recent past, a M_w 6.2 earthquake occurred on August 14 2003 offshore the NW coast of Lefkada, and caused landslides, rockslides and rockfalls along the western coast of the island (Karakostas et al. 2004, Papathanasiou et al., 2012). Significant damage was reported, particularly in the town of Lefkada, where a PGA of 0.42g was recorded.

On November 17th 2015, an M_w 6.5 earthquake struck the island of Lefkada and triggered a number of landslides, rockfalls and some structural damage. The most affected area by large rockslides was the western coast of the island, especially along its central and south portion, which are popular summer tourist destinations (Zekkos et al., 2017). The coseismic landslides completely covered the majority of the west coast beaches and damaged access roads.

On the southeast side of Lefkada, near the Gulf of Vassiliki, a seismically-triggered rockfall in Ponti village was responsible for one of two deaths caused by the earthquake (Figure 1). Of particular interest, is the very long travel path of the rock block, which was about 800 m in plan view from the point of detachment to the end of its path. Near the end of the rock fall path, the block impacted a family residence, penetrated two brick walls and killed a person in the house. The block exited through the back of the house and came to rest in the property's backyard.

The Ponti village rockfall site is a characteristic example of how seismically-induced rockfalls impact human activities. It also provides an opportunity to evaluate 2D and 3D rockfall analysis to predict details of the rockfall trajectory, based on field evidence. In order to create a highly accurate model of the rockfall propagation in 2D and 3D space, the rock path and the impact points on the slope were identified by a field survey. The study was performed using an Unmanned Aerial Vehicle (UAV) with an ultra-high definition (UHD) camera, which produced a high-resolution orthophoto and a Digital Terrain Model (DTM) of the slope. The orthophoto was used to identify the rolling section and the impact points of the rock along its trajectory, which were verified by field observation. The high-resolution DTM made it possible to conduct kinematic rebound analysis and a 3D rockfall analysis.

2.   Ponti rockfall - site conditions

The locations of the epicenters of the 2003 and 2015 events, as well as the location of the rockfall case study are shown in Figure 1. The southwest coast of Lefkada is part of the Triassic to Eocene age Paxos zone and consists of limestones and dolomites that are covered by Neogene clastic sedimentary rocks, mostly sandstones and marls. Figure 1 also shows faults and high rockfall hazard areas as identified by Rondoyanni et al. (2007). The rockfall at Ponti is not located in an identified high rockfall hazard area. Based on measurements conducted at one location along the rockfall path using the Multichannel Analysis of Surface Waves method, the in-situ

84 shear wave velocity of the top layer was estimated to be around 800 m/s, which is a

85 high velocity and is consistent with the limestone rock at the site.

86 The slope overhanging Ponti village (shown in Fig. 2) has a maximum height of 600

87 m and an average slope angle of 35^0 to 40^0. The geological formations at the Ponti

88 rockfall site are limestones covered by moderately cemented talus materials. The

89 thickness of the talus materials, when present, ranges between 0.5 and 4.0 m.

90 Several detached limestone blocks were identified on the scree slope, with volumes

91 between 0.5 and 2 m^3. Based on the size distribution of these rocks on the slope, the

92 average expected block volume would be in the order of 1 to 2 m^3.

93 The rockfall release area was at an elevation of 500 m, while the impacted house

94 (shown in Figure 3) at an elevation of 130 m. The volume of the detached limestone

95 block was approximately 2 m^3 and its dimensions equal to 1.4 m x 1.4 m x 1 m.

96 There was no previously reported rockfall incident at Ponti that impacted the road or

97 a house.

3.   UAV mapping

3.1.   Introduction

100 A quadrotor UAV (Phantom 3 professional) was deployed to reach the uphill terrrain

101 that was practically inaccessible. The UAV was equiped with an Ultra-high definition

102 (UHD) 12 MP camera and had the capacity to collect 4K video. The sensor was a

103 1/2.3" CMOS (6.47x3.41mm) and the effective pixel resolution was 12.4 MP

104 (4096x2160 pixels). An immediate UAV data acquisition expedition was conducted 2

105 days after the earthquake. A second more detailed mapping UAV expedition with the

106 objective to create a DTM was conducted 5 months after the rockfall event.

107 The first objective of the UAV deployment was to find the inititiation point of the rock

108 and then identify the rockfall path (shown in Figure 2). A particular focus on that part

109 of the task was the identification of rolling and bouncing sections of the rockfall path.

110 In addition, to generate a high-resolution orthophoto of the rockfall trajectory, aerial

111 video imagery was collected, and the resulting digital surface model (DSM) and

112 digital terrain model (DTM) was used to perform rockfall analysis.

113 The aerial survey was conducted by capturing 4K video along a gridded pattern

114 covering the area of interest, at a mean flight altitude of 115m above the terrain

115 resulting image frames of a mean ground sampling distance (GSD) of

116 4.97cm/pix.The overlap between image frames was minimum frontal 80%, side 65%

117 and a total of 714 camera stations (video frames extracted) were included as shown

118 in Figure 4.

119 The Structure-from-Motion (SfM) methodology was implemented to create a 3D

120 point cloud of the terrain and develop a 3D model. The methodology is based on

121 identifying matching features in multiple images, and thus imagery overlap of at least

122 70% is required. Compared to classic photogrametry methodologies, where the

123 location of the observing point is well established, SfM tracks specific discernible

124 features in multiple images, and through non-linear least-squares minimisation

125 (Westoby et al., 2012), iteratively estimates both camera positions, as well as object

126 coordinates in an arbitrary 3D coordinate system. In this process, sparse bundle

127 adjustment (Snavely et al., 2008) is implemented to transform measured image

128 coordinates to three dimensional points of the area of interest. The outcome of this

129 process is a sparse 3D point cloud in the same local 3D coordinate system

130 (Micheletti et al., 2015). Subsequently, through an incremental 3D scene

131 reconstruction, the 3D point cloud is densified. Paired with GPS measurements of a

132 number of control points (for this site, 10 fast-static GPS points were collected) at the

133 top, middle and bottom of the surveyed area, the 3D point cloud is georeferenced to

134 a specific coordinate system and through post-processing a digital surface model

135 (DSM), a digital terrrain model (DTM) and orthophotos are created. The SfM

136 methodology was implemented in this study using the Agisoft Photoscan software.

137 Precalibrated camera parameters by the SfM software (Photoscan) were introduced

138 and then optimized during the matching process and the initialization of Ground

139 Control Points.

140 In addition, the accuracy of the model has been examined by using portions of the

141 ground control points and developing DTM of differencing between different models,

142 an investigation that is described by Manousakis et al. (2016). Finally, a comparison

143 was made of the DTM developed by the UAV against the satellite-based DTM used

144 for the Greek cadastre. The two surfaces were found to be very similar, as discussed

145 subsequently.

146 **3.2.   High-resolution Orthophoto**

147 A 5cm pixel size orthophoto was generated based on the methodology outlined

148 earlier. As shown in Figure 5, the rolling section and the bouncing locations of the

149 rock block throughout its course were identified. The rolling section was easily

150 discerned as a continuous and largely linear mark left in the vegetated terrain. Impact

151 points that are part of the bouncing section of the rock, were identified as circular to

152 ellipsoidal bare earth craters with no disturbance in between. The last bouncing point

153 before impacting the house is clearly identified on the paved road. The plan view

154 ortho-imagery, along with the original footage of the video collected was crucial to the

155 qualitative identification of these features. The alternative, i.e., land-based,

156 conventional field reconnaissance was physically impossible to perform throughout

157 the vegetated and steep terrain.

158 **3.3.   Digital Surface Model and Digital Terrain Model**

159 A profile section and a 10 cm Digital Surface Model (DSM) were then developed

160 (Manousakis et al., 2016) allowing the identification of features such as structures,

161 slope benches or high trees, which could affect the rock's path downhill.

162 Subsequently, this resolution of the DSM proved to be not only unnecessarily high

163   and thus difficult to manipulate in subsequent rockfall analyses, but also caused

164   numerical instabilities in the rockfall analyses. Therefore, a downscaled 2 m DTM

165   was produced for the rockfall analysis as described next. First, an aggregate

166   generalization scheme where each output cell is assigned the minimum elevation of

167   the input cells that are encompassed by that cell. In addition, noise filtering and

168   smoothing processing were implemented to reduce the effect of vegetation in the

169   final rasterized model. Note that this resolution is still higher than the resolution of

170   DTM that are often used in rockfall analyses.

171   To create the DTM, algorithms for vegetation removal were executed using

172   Whitebox GAT Geospatial Analysis Tools platform (Lindsay, 2016) .. The process

173   involves Point Cloud neighborhood examination and DEM smoothing algorithms.

174   Firstly, a bare-Earth digital elevation model (DEM) was interpolated from the input

175   point cloud LAS file, by specifying the grid resolution (2m) and the inter-point slope

176   threshold. The algorithm distinguished ground points from non-ground points based

177   on the inter-point slope threshold. Thus, the interpolation area was divided into lattice

178   cells, corresponding to the grid of the output DEM. All of the point cloud points within

179   the circle containing each grid cell were then examined as a neighborhood. Those

180   points within a neighborhood that have an inter-point slope with any other point and

181   are also situated above the corresponding point, are attributed as non-ground points.

182   An appropriate value for the inter-point slope threshold parameter depends on the

183   steepness of the terrain, but generally values of 15-35 degrees produce satisfactory

184   results. The elevation assigned to the grid cell was then the nearest ground point

185   elevation (Lindsay, 2016.).

186   Further processing of the interpolated bare-earth DEM was executed to improve

187   vegetation and structures removal results by applying a second algorithm to point

188   cloud DEMs, which frequently contain numerous off-terrain objects such as buildings,

189   trees and other vegetation, cars, fences and other anthropogenic objects. The

algorithm works by locating and removing steep-sided peaks within the DEM. All peaks within a sub-grid, with a dimension of the user-specified Maximum Off-Terrain Object (OTO) Size, in pixels, were identified and removed. Each of the edge cells of the peaks were then queried to check if they had a slope that is less than the user-specified Minimum OTO Edge Slope and a back-filling procedure was used. This ensured that natural topographic features such as hills are not recognized and confused as Off-Terrain features (Whitebox GAT help topics).

The final DTM model had a total RMS error after filtering for 6 GCPs was 0.07m, while total RMS error for 4 Check Points was 0.20m. When compared to a 5m DEM from Greek National Cadastre with a geometric accuracy of RMSEz ≤ 2,00m and absolute accuracy ≤ 3,92m for a confidence level of 95%, a mean difference of 0.77 m and a standard deviation of 1.25 m is observed, which is well into the range of uncertainty of the cadastre model itself.

4.   Earthquake characteristics – Initial conditions

4.1.   Seismic acceleration

The epicenter of the earthquake according to the National Observatory of Athens, Institute of Geodynamics (NOA) is located onshore near the west coast of Lefkada. The causative fault is estimated to be a near-vertical strike-slip fault with dextral sense of motion (Ganas et al., 2015, 2016). Based on the focal mechanism study of the earthquake, it was determined that the earthquake was related to the right lateral Kefalonia-Lefkada Transform Fault (KLTF), which runs nearly parallel to the west coasts of both Lefkada and Kefalonia island, in two segments (Papazachos et al. 1998, Rondoyanni et al. 2012).

A strong motion station recorded the ground motions in the village of Vasiliki located at a distance of 2.5 km from the Ponti rockfall site. The ground motion characteristics

216   of the recording are summarized in Table 1 and are presented in Figure 6 (ITSAK,

217   2016).

4.2.   Topography effect

219   Peak ground acceleration (PGA) along the rock slope is estimated from the PGA of

220   the base (PGA$_b$) modified by site and topographic effects (Mavrouli et al., 2009). In

221   the present case, local shaking intensity in terms of horizontal PGA was considered.

222   The E-W component of acceleration was considered for the determination of the

223   initial velocity. The peak ground acceleration on the slope face (PGA$_{sf}$) was

224   considered equal to the acceleration at the slope crest (PGA$_{cr}$). The acceleration at

225   the base was equal to 0.32g and thus at the crest PGA$_{cr}$= 1.5 PGA$_b$ was equal to

226   0.48g.

4.3.   Initial velocity of rock block

228   The initial horizontal velocity of the block, at the time of detachment, was calculated

229   considering equilibrium of the produced work and the kinetic energy according to

230   equation 1.

231    $$v_x = \sqrt{2 \times PGA_{sf} \times s} \quad (1),$$

232   where PGA$_{sf}$ is the acceleration on the slope at the location of detachment and s the

233   initial displacement of the block in order to initiate its downslope movement.

234   The initial horizontal velocity was calculated equal to 0.67 m/s, considering a

235   displacement in the order of s = 0.05 m. The vertical component of the initial velocity

236   is assumed to be zero.

5.   Trajectory analysis

238   In order to estimate the possible rock paths and design remedial measures,

239   simulation programs based on lumped-mass analysis models are commonly used in

240   engineering practice. The trajectory of a block is modelled as a combination of four

241 motion types; free falling, bouncing, rolling and sliding (Descoeudres and

242 Zimmermann, 1987). Usage of the lump-mass model has some key limitations; the

243 block is described as rigid and dimensionless with an idealized shape (sphere);

244 therefore the model neglects the block's actual shape and configuration at impact,

245 even though both affect the resulting motion.

246 **5.1.   Modelling the response to an impact**

247 The most critical input parameters are the coefficients of restitution (COR), which

248 control the bouncing of the block. In general, the coefficient of restitution (COR) is

249 defined as the decimal fractional value representing the ratio of velocities (or

250 impulses or energies; depending on the definition used) before and after an impact of

251 two colliding entities (or a body and a rigid surface). When in contact with the slope,

252 the block's magnitude of velocity changes according to the COR value. Hence, COR

253 is assumed to be an overall value that takes into account all the characteristics of the

254 impact; including deformation, sliding upon contact point, transformation of rotational

255 moments into translational and vice versa (Giani, 1992).

256 The most widely used definitions originate from the theory of inelastic collision as

257 described by Newtonian mechanics. For an object impacting a rocky slope (Figure 7),

258 which is considered as a steadfast object, the kinematic COR (v_{COR}) is defined

259 according to Eq. 2.

$$v_{COR} = \frac{v_r}{v_i}$$

260   (2)

261 where v is the velocity magnitude and the subscripts i and r denote the trajectory

262 stage; incident (before impact) and rebound (after impact) respectively.

263 Two different mechanisms participate in the energy dissipation process; energy loss

264 normal to the slope is attributed to the deformation of the colliding entities, and in the

265 tangential direction is due to friction between them. Therefore kinematic COR has

266 been analyzed to the normal and tangential component with respect to the slope

267   surface, defining the normal (n_{COR}) and the tangential (t_{COR}) coefficient of restitution

268   (Eq. 3 and 4 respectively).

269 $$n_{COR} = \frac{v_{n,r}}{v_{n,i}} \qquad (3)$$

270   and

271 $$t_{COR} = \frac{v_{t,r}}{v_{t,i}} \qquad (4)$$

272   where the first subscript, n or t denotes the normal or the tangential components of

273   the velocity respectively.

274   Normal and tangential COR have prevailed in natural hazard mitigation design via

275   computer simulation due to their simplicity. Values for the coefficients of restitution

276   are acquired from values recommended in the literature (e.g., Azzoni et al. 1995;

277   Heidenreich 2004; Richards et al. 2001, RocScience, 2004). These values are mainly

278   related to the surface material type and originate from experience, experimental

279   studies or back analysis of previous rockfall events. This erroneously implies that

280   coefficients of restitution are material properties. However, COR values depend on

281   several parameters that cannot be easily assessed. Moreover, values suggested in

282   the literature vary considerably and are sometimes contradictory.

283   **5.2.   Rockfall path characteristics**

284   23 impact points were identified on the slope surface (Figure 8). Their coordinates

285   are presented in Table 2, along block's path starting from the detachment point

286   (where x=0). No trees were observed along the block's path.

287   The apparent dip of the slope at impact positions was measured from the DTM; on

288   each impact point a line was set with a length twice the block's mean dimension,

289   oriented according to preceding trajectory direction. Moreover, the impact point was

290   expanded on the DTM to a rectangular plane with a side twice the mean dimension

291   of the block (Figure 9). This plane was then oriented so that one side coincides with

292   the strike direction and its vertical side towards the dip direction. Thus, direction

293   difference, $\Delta\varphi$, was measured by strike direction and the preceding path and

294   deviation, e, was measured as the angle between pre- and post- impact planes

295   (Asteriou & Tsiambaos, 2016).

296   Having a detailed field survey of the trajectory path, a back analysis according to the

297   fundamental kinematic principles was performed with the intent to back-calculate the

298   actual COR values.

299   **5.3.   Kinematic analysis and assumptions**

300   The 23 impact points identified on the slope comprise a rockfall path of 22 parabolic

301   segments. The vertical and horizontal length of each segment is acquired by

302   subtracting consecutive points. Since no external forces act while the block is mid-air,

303   each segment lays on a vertical plane and is described by the general equation of

304   motion as:

$$y = x\tan\vartheta - \frac{gx^2}{2v_i^2\cos^2\vartheta}$$

305   (5)

306   where: θ the launch angle from the horizon and v the launch (initial) velocity (Figure

307   10).

308   Since no evidence can be collected regarding launch angle and velocity, innumerable

309   parabolas satisfy Eq. 5. However, θ is bound between –β and 90$^{\text{o}}$, so in order to

310   acquire realistic values for the initial velocity, its sensitivity for that given range was

311   investigated.

312   For the case presented in Fig. 11 (the first parabolic segment) it is shown that for the

313   majority of the release angles, initial velocity variation is low and ranges between 7.2

314   and 12 ms^{-1}. Additionally, the relationship between release angle and initial velocity is

315   expressed by a curvilinear function, with a minimum initial velocity value along with

316   an associated release angle (denoted hereafter as θ_{cr}).

317   Given the minimum initial velocity and the critical release angle for each parabolic

318   segment, the impact velocity and impact angle can be calculated. Subsequently,

319   normal and tangential velocity components according to the apparent dip of the

320   impact area, are calculated in order to evaluate COR values. Results are

321   summarized in Table 3.

322   **5.4.   Coefficients of restitution**

323   It is observed that v_{cor} (Table 3) is greater than one in 5 out of 22 impacts. According

324   to Eq. 3, this can only be achieved when impact velocity is less than rebound

325   velocity. However, this indicates that energy was added to the block upon impact,

326   which is not possible according to the law of conservation of energy. Thus, impact

327   velocity should be greater, which is possible if the launch velocity of the previous

328   impact was higher than the assumed minimum.

329   For the cases where $V_{cor}<1$, it is observed that kinematic COR ranges between 0.55

330   and 1.0 and presents smaller variation compared to normal or tangential coefficient

331   of restitution, similar to what was previously reported in relevant literature (i.e.

332   Asteriou et al, 2012; Asteriou & Tsiambaos, 2016).

333   The wide scatter of normal COR implies that the restitution coefficient cannot be a

334   material constant. Yet, in most relevant software, normal COR is defined solely by

335   the slope material. Moreover, normal COR values higher than one were calculated in

336   11 out of the 15 remaining impacts. Normal COR higher than one have been

337   observed in both experimental (e.g. Spadari et al., 2011; Buzzi et al., 2012; Asteriou

338   et al., 2012) and back-analysis studies (e.g. Paronuzzi, 2009) and are related to

339   irregular block shape and slope roughness, as well as to shallow impact angle and

340   angular motion. A more detailed presentation of the reasons why normal COR

341 exceeds unity can be found in Ferrari et al. (2013). However, in rockfall software

342 used in engineering practice, normal COR values are bounded between 0 and 1.

343 As shown in Figure 12, normal COR increases as the impact angle reduces, similarly

344 to previous observations by Giacomini et al. (2012), Asteriou et al. (2012) and Wyllie

345 (2014). The correlation proposed by Wyllie (2014) is also plotted in Figure 13 and

346 seems to describe consistently, but on the unconservative side, the trend and the

347 values acquired by the aforementioned analysis and assumptions.

348 6. Rockfall modelling

349 6.1. 2-D analyses

350 A deterministic 2D rockfall analysis was first performed using Rocfall software

351 (RocScience, 2004). According to Asteriou & Tsiambaos (2016) the most important

352 influence is posed by the impact configuration, which is influenced by slope

353 roughness and block shape. In this study, roughness has been fully taken into

354 account (considering the block's dimension scale) by the high resolution of the

355 cross-section used in the analyses (more than 1500 x-y points were used –

356 approximately 2 points per meter). Based on our experience, this resolution is

357 significantly higher compared to other rockfall studies. Moreover, it was not possible

358 to simulate block shape effect, nor the configuration of the block at impact, using

359 lumped-mass model analysis.

360 Considering an initial velocity of 0.67 m/sec, according to the numerical analyses, the

361 falling rock primarily rolls on the slope and stops much earlier than its actual (field-

362 verified) run out distance, approximately 400 m downslope from its initiation point

363 (Fig. 8; case 1). The restitution coefficients were n_{COR}=0.35, t_{COR}=0.85, and were

364 selected based on the suggested values for bedrock outrcrops provided in the

365 software documentation.

366 Note that for this analysis, the friction angle was set to zero. A standard deviation for

367 the coefficients of restitution, the friction angle and roughness of the material on the

368   slope was not used for this deterministic analysis. For friction equal to 32^0 (as

369   suggested by the software documentation), the rock travels downslope only 50 m.

370   Additional analysis was also performed, with lower coefficients of restitution that are

371   representative of the talus material on the slope (n_{COR}=0.32, t_{COR}=0.82, φ=30^0) per

372   the software documentation. In this case, the rock block rolled only a few meters

373   downslope. Therefore, it is evident that the actual rock trajectory cannot be

374   simulated.

375   In order to more closely simulate the actual trajectory, various combinations of

376   restitution coefficients and friction angle were considered. The closest match

377   occurred for n_{COR}=0.60 and t_{COR}=0.85, while the friction angle was set to zero and no

378   velocity scaling was applied. For these input parameters, the rock block reaches the

379   house with a velocity of 18 m/s approximately (Fig. 8; case 2). These values for the

380   restitution coefficients correspond to a bedrock material (limestone).

381   In this case, the modelled trajectory is significantly different from the actual one. The

382   main difference is that the block rolls up to 200 m downslope while the actual rolling

383   section is 400 m (as shown in Figure 8). Furthermore the impacts on the ground in

384   the bouncing section of the trajectory are considerably fewer in number (14 versus

385   23) and in different locations compared to the actual ones. Finally, the bounce height

386   of some impacts seems unrealistically high. For example, the 2nd bounce has a jump

387   height (f) of ~17.5m over a length (s) of ~50m, resulting to a f/s ratio of ~1/3, when

388   the characteristic f/s ratios for high, normal and shallow jumps is 1/6, 1/8 and 1/12

389   respectively, as suugested by Volkwein et al. (2011).

390   **6.2.   3-D rockfall analysis**

391   The rockfall trajectory model Rockyfor3D (Dorren, 2012) has also been used in order

392   to validate the encountered trajectory and assess the probability that the falling rock

393   (from the specific source area) reaches the impacted house.

394   The 3D analysis was based on the down-scaled 2 m resolution Digital Terrain Model

395   (DTM) that was generated from the 10 cm DSM. The following raster maps were

396   developed for the 3D analysis: a) rock density of rockfall source, b) height, width,

397   length and shape of block, c) slope surface roughness and d) soil type on the slope,

398   which is directly linked with the normal coefficient of restitution, n_{COR}.

399   The slope roughness was modeled using the mean obstacle height (MOH), which is

400   the typical height of an obstacle that the falling block encounters on the slope at a

401   probability of 70%, 20% and 10% of the trajectories (according to the suggested

402   procedure in Rockyfor3D). No vegetation was considered in the analysis, which

403   favours a longer trajectory. The parameters considered in the 3D analysis for the

404   different formations are summarised in Table 4. The spatial occurrence of each soil

405   type is shown in Figure 13 and the assigned values of n_{COR} are according to the

406   Rockyfor3D manual. The values for soil type 4.1 in Figure 13 are slightly different

407   from those of soil type 4 (proposed in the manual), denoting talus with a larger

408   percentage of fallen boulders. The block dimensions were considered equal to 2 m^3

409   and the shape of the boulder was rectangle. In order to simulate the initial velocity of

410   the falling rock due to the earthquake, an additional initial fall height is considered in

411   the analysis, which for this case was set equal to 0.5 m.

412   The energy line angles were recalculated from the simulated trajectories and it was

413   determined that the energy line angle with highest frequency (39%) was 30-31^0.

414   Based on the 3D analysis no rock blocks would impact the house, although the rock

415   paths are closer to the actual trajectories compared to RocFall software. The reach

416   probability of the falling rocks, initiating from the source point, is shown in Figure 14.

417   Reach probability is the percentage of the falling rocks in relation to the total number

418   of falling rocks that reach a specific point along the line of the trajectory.

419   **6.3.   Lateral dispersion & Deviation**

420   Lateral dispersion is defined as the ratio between the distance separating the two

421   extreme fall paths (as seen looking at the face of the slope) and the length of the

422   slope (Azzoni and de Freitas 1995). According to Crosta and Agliardi (2004) the

423   factors that control lateral dispersion are (a) macro-topography factors, factors

424   related to the overall slope geometry; (b) micro-topography factors controlled by the

425   slope local roughness; and (c) dynamic factors, associated with the interaction

426   between slope features and block dynamics during bouncing and rolling. Based on

427   an experimental investigation, Azzoni and de Freitas (1995) noted that the dispersion

428   is generally in the range of 10% to 20%, regardless of the length of the slope and that

429   steeper slopes exhibit smaller dispersion. Agliardi and Crosta (2003) calculated

430   lateral dispersion to be up to 34%, using high-resolution numerical models on natural

431   rough and geometrically complex slopes.

432   Lateral dispersion cannot be defined from the actual rockfall event in Ponti since only

433   one path is available. Using the simulated trajectories from RockyFor3D, which are in

434   the 3d space (Figure 15), a lateral dispersion of approximately 60% is shown in the

435   middle of the distance between detachment point and the house. This is significantly

436   higher dispersion than the findings of Azzoni and de Freitas (1995) and Agliardi and

437   Crosta (2003). The lateral dispersion computed by RockyFor3D is extremely

438   pronounced and most likely due to the topography effect of the area of detachment.

439   Specifically, the origin of the rock block is located practically on the ridgeline,

440   facilitating the deviation of the rock fall trajectory from the slope line.

441   Asteriou & Tsiambaos (2016) defined deviation (e) as the dihedral angle between the

442   pre- and post-impact planes that contain the trajectory. They found that deviation is

443   controlled by the direction difference $\Delta\varphi$, the slope inclination and the shape of the

444   block. For a parallel impact (i.e. $\Delta\varphi=0^0$) a spherical block presents significantly less

445   deviation compared to a cubical. Additionally, deviation is equally distributed along

446   the post-impact direction and reduces as the slope's inclination increases. On oblique

447   impacts, the block's direction after impact changes towards the slope aspect and as

448    $\Delta\varphi$ increases, this trend becomes more pronounced.

449   Figure 16 illustrates the relationship of deviation with direction difference. It is noted

450   that for parallel impacts ($\Delta\varphi=0^0$), deviation is uniformly distributed along the post-

451   impact direction. As direction difference increases, deviation becomes positive, which

452   means that the change of direction is following the direction of slope's aspect. These

453   findings are consistent with trends described by Asteriou & Tsiambaos (2016), but

454   the deviation of the actual trajectory is significantly lower. This can be attributed to

455   the different conditions (i.e. block shape, slope material, slope roughness, incident

456   velocity and angle, and scale) between the experimental program conducted by

457   Asteriou & Tsiambaos (2016) and the Ponti rockfall event.

458   **7.   Conclusions**

459   UAV-enabled reconnaissance was successfully used for the identification of the

460   origin of the detached rock, the rockfall trajectory and the impact points on the slope,

461   and especially discerning the rolling and bouncing sections of the trajectory. A UAV

462   with an ultra-high definition (UHD) camera was deployed to reach the inaccessible,

463   steep and partly vegetated uphill terrain. A high-resolution orthophoto of the rockfall

464   trajectory, a 10 cm DSM and a 2 m DTM were generated and formed the basis for an

465   analytical 2D kinematic analysis and a comparison with the outcomes of 2D and 3D

466   rockfall analysis software.

467   The initial velocity of the detached rock was estimated based on site conditions and

468   amplification of the ground acceleration due to topography. It was found that the

469   initial velocity of the blocks plays a significant role in the accurate re-production of the

470   rockfall trajectory.

471   Based on the computational analysis performed, it was found that the coefficients of

472   restitution cannot be directly connected to the material type, nor can be considered

473   material constants. The impact angle seems to influence the normal COR, which has

474   been also observed in other recent studies, but has not been incorporated yet on

475   analysis models.

476   It was proven impossible to replicate the actual trajectory of the rock fall by

477   performing a 2D rockfall analysis with the recommended set of parameters indicating

478   limitations in the present formulations. In an attempt to match the actual rock path to

479   the analysis output, the friction angle of the limestone slope was considered equal to

480   zero. However, the falling rock still rolled on the slope and stopped much earlier than

481   its actual runout distance while the impacts on the ground in the bouncing section of

482   the trajectory were considerably different in number and in location compared to the

483   actual ones.

484   Using the 3D analysis software and recommended input parameters, rock trajectories

485   better approximated the actual trajectory indicating that the 3D analysis can be more

486   accurate than the 2D analysis.

487   Based on the aforementioned analyses it becomes evident that engineering

488   judgement and experience must accompany the usage of commercial rockfall

489   software in order to acquire realistic paths. One should never blindly use the

490   recommended set of parameters since field performance can differ significantly, as

491   demonstrated by this case study.

492

References

494   1. Agliardi F, Crosta GB (2003) High resolution three-dimensional numerical

495   modelling of rockfalls. International Journal of Rock Mechanics and Mining

496   Sciences 40:455-471. doi: 10.1016/S1365-1609(03)00021-2

497   2. Asteriou P, Saroglou H, Tsiambaos G (2012). Geotechnical and kinematic

498   parameters affecting the coefficients of restitution for rock fall analysis.

499   International Journal of Rock Mechanics and Mining Sciences 54:103-113.

500   doi:10.1016/j.ijrmms.2012.05.029.

501 3. Asteriou P and Tsiambaos G. (2016). Empirical Model for Predicting Rockfall

502   Trajectory Direction. Rock Mechanics and Rock Engineering 49.3, pp. 927–

503   941.

504 4. Azzoni A, de Freitas MH (1995). Experimentally gained parameters, decisive

505   for rock fall analysis. Rock Mechanics and Rock Engineering 28:111-124. doi:

506   10.1007/BF01020064

507 5. Buzzi O, Giacomini A, Spadari M (2012) Laboratory investigation on high

508   values of restitution coefficients. Rock Mechanics and Rock Engineering

509   45:35-43

510 6. Crosta GB, Agliardi F (2004) Parametric evaluation of 3D dispersion of

511   rockfall trajectories. Natural Hazards and Earth System Science 4:583-598.

512   doi:10.5194/nhess-4-583-2004

513 7. Descoeudres F, Zimmermann TH. Three-dimensional dynamic calculation of

514   rockfalls. In: Proceedings of the 6th International Congress on Rock

515   Mechanics. Montreal; 30 August -3 September 1987. p. 337–42.

516 8. Dorren, L.K.A., 2012. Rockyfor3D (v5.1) revealed - Transparent description of

517   the complete 3D rockfall model. ecorisQ paper, 31 p.

518 9. Ganas, A., Briole, P., Papathanassiou, G., Bozionelos, G., Avallone, A.,

519   Melgar, D., Argyrakis, P., Valkaniotis, S., Mendonidis, E., Moshou, A. and

520   Elias, P. (2015). A preliminary report on the Nov 17, 2015 M=6.4 South

521   Lefkada earthquake, Ionian Sea, Greece, Report to EPPO, December 4

522   2015.

523 10. Ganas A., Elias P., Bozionelos G., Papathanassiou G., Avallone A.,

524   Papastergios P. Valkaniotis S., Parcharidis I., Briole P. (2016). Coseismic

deformation, field observations and seismic fault of the 17 November 2015 M = 6.5, Lefkada Island, Greece earthquake. Tectonophysics 687, pp. 210–222.

11. Giani GP. Rock Slope Stability Analysis. Rotterdam: Balkema A.A; 1992.

12. Giacomini A, Thoeni K, Lambert C, Booth S, Sloan SW (2012) Experimental study on rockfall drapery systems for open pit highwalls. International Journal of Rock Mechanics and Mining Sciences 56:171-181. doi:10.1016/j.ijrmms.2012.07.030

13. Ferrari F, Giani GP, Apuani T (2013) Why can rockfall normal restitution coefficient be higher than one? Rendiconti Online Societa Geologica Italiana 24

14. Heidenreich B (2004) Small- and half-scale experimental studies of rockfall impacts on sandy slopes. Dissertation, EPFL.

15. ITSAK (2016). Preliminary presentation of the main recording of ITSAK – OASP accelerometer network in Central Ionian. Earthquake M6.4 17/11/2015. Thessaloniki, 11 pp.

16. Karakostas, V. G., Papadimitriou, E. E., and Papazachos, C. B. 2004. Properties of the 2003 Lefkada, Ionian Islands, Greece, Earthquake Seismic Sequence and Seismicity Triggering. Bulletin of the Seismological Society of America, 94 (5), 1976–1981, October 2004

17. Lindsay JB. 2016. Whitebox GAT: A case study in geomorphometric analysis. Computers & Geosciences, 95: 75-84. DOI: 10.1016/j.cageo.2016.07.003

18. Manousakis J., Zekkos D., Saroglou H., Clark M. (2016). Comparison of UAV-enabled photogrammetry-based 3D point clouds and interpolated DSMs of sloping terrain for rockfall hazard analysis. Proc. Int. Archives of the Photogrammetry, Remote Sensing and Spatial Information Sciences, Vol. XLII-2/W2, p. 71-78.

551   19. Marinos P, Tsiambaos G., 2002. Earthquake triggering rock falls affecting

552   historic monuments and a traditional settlement in Skyros Island, Greece.

553   Proc. of the Int. Symposium: Landslide risk mitigation and protection of

554   cultural and natural heritage, Kyoto, Japan, pp. 343-346.

555   20. Mavrouli O., Corominas J., Wartman J. (2009). Methodology to evaluate rock

556   slope stability under seismic conditions at Sol`a de Santa Coloma, Andorra.

557   Nat. Hazards Earth Syst. Sci., 9, 1763–1773.Micheletti N., Chandler J., Lane

558   S., 2015. Structure from Motion (SfM) Photogrammetry. British Society for

559   Geomorphology. *Geomorphological Techniques*, Chap. 2, Sec. 2.2 (2015)

560   22. Papathanassiou, G., Valkaniotis, S., Ganas, A. and Pavlides, S. 2012. GIS-

561   based statistical analysis of the spatial distribution of earthquake-induced

562   landslides in the island of Lefkada, Ionian Islands, Greece, Landslides,

563   Journal of the International Consortium on Landslides,DOI 10.1007/s10346-

564   012-0357-1

565   23. Papazachos B.C., Papadimitriou E.E., Kiratzi A.A., Papazachou C.B., Louvari

566   E.K. 1998. Fault plane solutions in the Aegean sea and the surrounding area

567   and their tectonic implication. Bull Geof Teor Appl 39(3), 199–218.

568   24. Paronuzzi P. (2009) Field Evidence and Kinematical Back-Analysis of Block

569   Rebounds: The Lavone Rockfall, Northern Italy. *Rock Mech Rock Eng*,

570   42:783–813

571   25. Richards LR, Peng B, Bell DH (2001) Laboratory and field evaluation of the

572   normal Coefficient of Restitution for rocks. Proceedings of ISRM Regional

573   Symposium EUROCK2001:149-155

574   26. RocScience, 2004. Rocfall Manual.

575   27. Rondoyanni Th., Mettos A., Paschos P., Georgiou Ch. 2007. Neotectonic

576   map of Greece, scale 1:100.000, Lefkada sheet. I.G.M.E., Athens.

577 28. Saroglou, H. 2013. Rockfall hazard in Greece. Bulletin of the Geological
578   Society of Greece, vol. XLVII, no3, 1429-1438.

579 29. Saroglou, H., Marinos, V., Marinos, P., Tsiambaos, G. 2012. Rockfall hazard
580   and risk assessment: an example from a high promontory at the historical site
581   of Monemvasia, Greece. Natural Hazards and Earth System Sciences, 12,
582   1823–1836. doi:10.5194/nhess-12-1823-2012.

583 30. Snavely N., Seitz S.N., Szeliski R., 2008. Modeling the world from internet
584   photo collections. *International Journal of Computer Vision* 80: 189-210.

585 31. Spadari M, Giacomini A., Buzzi O., Fityus S., Giani G.P.(2011). In situ rockfall
586   testing in New South Wales, Australia. Int J Rock Mech Mining Sci, 49, pp.
587   84–93.

588 32. Volkwein, A., Schellenberg, K., Labiouse, V., Agliardi, F., Berger, F., Bourrier,
589   F., Dorren, L. K. A., Gerber, W., and Jaboyedoff, M., 2011. Rockfall
590   characterisation and structural protection – a review, Nat. Hazards Earth Syst.
591   Sci., 11, 2617–2651, doi:10.5194/nhess-11-2617-2011.

592 35. Westoby M.J., Brasington J., Glasser N.F., Hambrey M.J., Reynolds J.M.,
593   2012. 'Structure-from-Motion' photogrammetry: A low-cost, effective tool for
594   geoscience applications. *Geomorphology* 179 (2012) 300-314.

595 36. Wyllie, D. C. (2014). Calibration of rock fall modeling parameters.
596   International Journal of Rock Mechanics and Mining Sciences 67: 170-180

597 37. Zekkos D., Clark M., Cowell K., Medwedeff W., Manousakis J., Saroglou H.
598   Tsiambaos G. (2017). Satellite and UAV-enabled mapping of landslides
599   caused by the November 17th 2015 M_w 6.5 Lefkada earthquake. Proc. 19th Int.
600   Conference on Soil Mechanics and Geotechnical Engineering, Seoul, 17-22
601   September 2017.

602

 TABLES

 Table 1. Accelerometer recordings

Component	Acceleration (cm/sec^2)	Velocity (cm/sec)	Displacement (cm)
NS-comp	363	59.3	21.27
EW-comp	327	34.1	14.01
Z-comp	256	17.7	6.56

604

605 Table 2. Impact points characteristics

Impact point	X (m)	Y (m)	app_dip (^{0})	Δφ (^{0})	e (^{0})
1	287.63	338	39.0	0	0
2	298.38	329.68	16.3	33	0
3	305.48	324.5	27.9	27	-1
4	321.54	314.83	41.0	11.6	0.5
5	365.34	287.6	30.4	11.9	0.3
6	373.32	284.85	39.7	10.6	1.8
7	425.1	261.64	14.7	6.6	-1.3
8	464.43	251.13	18.4	33.3	0.8
9	472.06	248.81	14.0	19.1	2.3
10	495.29	243.81	7.5	52.3	0.9
11	515.31	240.8	7.9	51	0.6
12	535.56	238.31	9.1	46.7	3
13	562.11	232.22	8.7	47.3	2.1
14	605.51	211.12	16.9	25.6	-1.7
15	619.1	204.48	27.1	4.6	-3
16	639.13	196.96	21.2	8	4.7
17	662.41	184	23.3	28.5	5.2
18	688.4	169.3	27.4	0.3	-2.5
19	712.23	157.67	25.4	0.5	0.1
20	745.28	143.16	21.9	0.5	-0.1
21	762.9	137.01	22.0	0.7	2
22	789.23	125.98	21.6	1.4	-0.8
23	801.53	132.75	8.4	0.2	0.1

606   Table 3. Parabolic paths characteristics for the minimum release velocity

Segment	Δx(m)	Δy (m)	θ_{cr} (^{0})	$v_{r,min}$	v_{impact}	a_i	v_{COR}	n_{COR}	t_{COR}
1-2	10.75	-8.33	26.8	7.19	13.19	44.5	0.55	0.71	0.31
2-3	7.1	-5.18	25.7	5.95	9.51	27.8	0.63	0.90	0.53
3-4	16.07	-9.66	31.5	9.45	12.68	9.6	0.75	3.86	0.38
4-5	43.79	-27.23	27.7	15.46	23.13	23.3	0.67	1.57	0.26
5-6	7.98	-2.75	35.7	7.47	10.49	14.9	0.71	2.52	0.30
6-7	51.78	-23.21	34.8	18.15	21.61	31.7	0.84	1.54	0.26
7-8	39.33	-10.5	35.9	17.23	24.01	36.1	0.72	0.94	0.56
8-9	7.63	-2.32	35.9	7.45	10.54	41.1	0.71	0.87	0.55
9-10	23.23	-5	40.5	13.58	13.12	30.7	1.03	1.65	0.70
10-11	20.02	-3.01	41.1	13.00	11.57	24.2	1.12	2.06	0.82
11-12	20.25	-2.49	40.9	13.26	11.22	17.6	1.18	2.94	0.82
12-13	26.55	-6.1	38.0	14.40	14.25	28.5	1.01	1.55	0.78
13-14	43.41	-21.1	32.9	16.33	25.70	40.9	0.64	0.64	0.63
14-15	13.59	-6.64	30.7	9.13	12.81	25.1	0.71	1.24	0.53
15-16	20.03	-7.52	33.8	11.67	15.42	29.8	0.76	1.33	0.42
16-17	23.27	-12.96	31.9	11.59	15.89	28.5	0.73	1.22	0.50
17-18	25.99	-14.7	29.9	12.20	20.11	30.9	0.61	0.95	0.42
18-19	23.83	-11.63	32.2	12.08	17.10	27.9	0.71	1.30	0.40
19-20	33.05	-14.51	33.6	14.55	20.62	32.1	0.71	1.14	0.43
20-21	17.62	-6.15	34.5	11.08	11.99	18.4	0.92	2.44	0.54
21-22	26.33	-11.03	35.1	13.11	16.33	27.3	0.80	1.47	0.49
22-23	12.3	6.77	58.1	14.30	13.97	48.9	1.02	1.34	0.28

607

608

608   Table 4. Restitution parameters for Rockyfor3D

Geological formation/ other	Mean n_{COR}	MOH			Soil type (Rockyfor3D)
		rg70	rg20	rg10	
Scree (Ø < ~10 cm), or medium compact soil with small rock fragments	0.33	0.03	0.05	0.05	3
Talus slope (Ø > ~10 cm), or compact soil with large rock fragments	0.38	0.05	0.1	0.2	4
Talus with fallen boulders	0.42	0.15	0.15	0.2	4.1
Bedrock with thin weathered material	0.43	0	0.05	0.1	5
Asphalt road	0.35	0	0	0	7

609

FIGURES
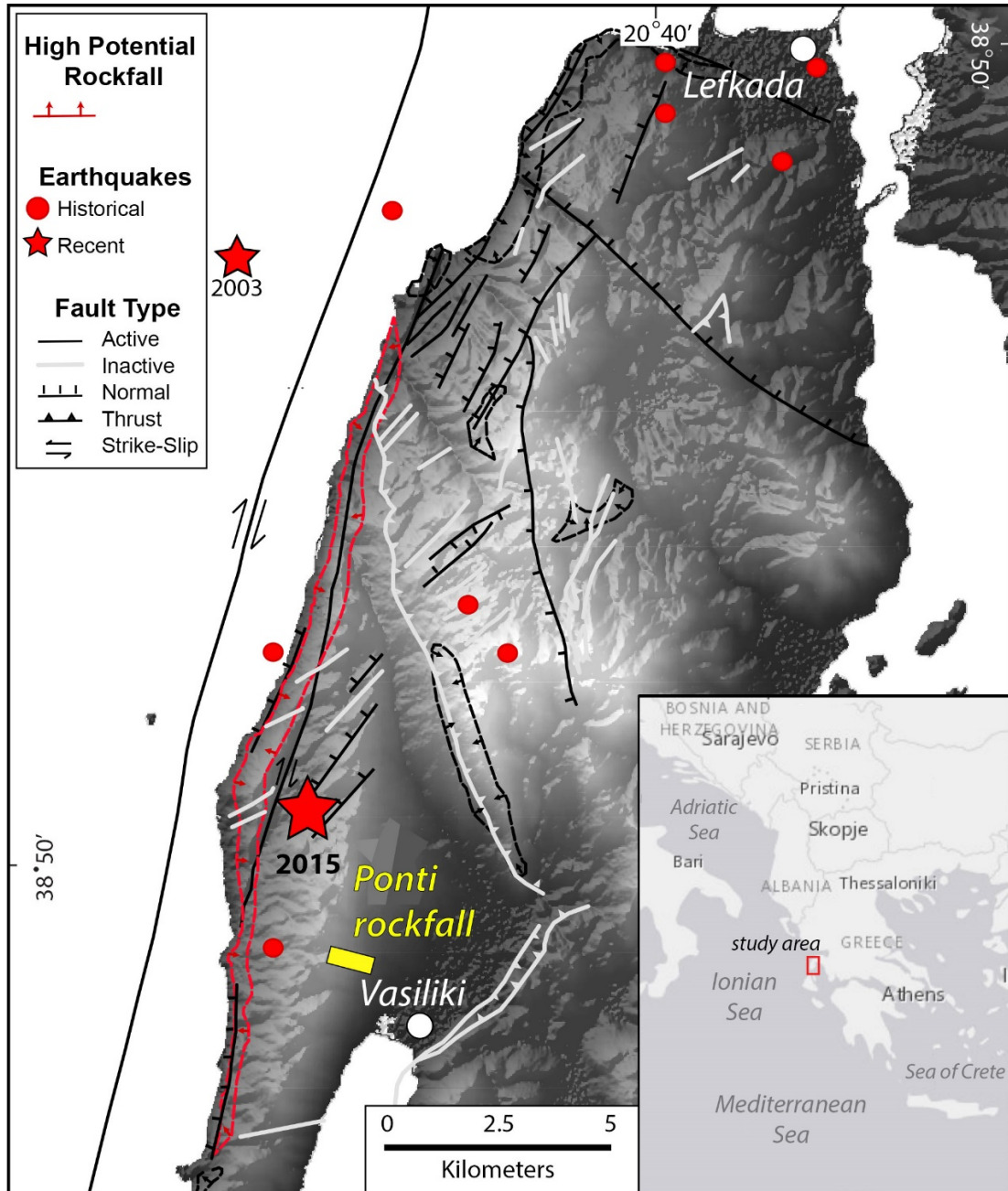
Figure 1. Map of Lefkada Island, Greece with location of study site (Ponti) and epicenters of recent earthquakes (stars) in 2003 (M_w6.2) and 2015 (M_w6.5), as well as historical ones (circles) Map also shows faults and high potential rockfall areas as identified by Rondoyanni et al. (2007).
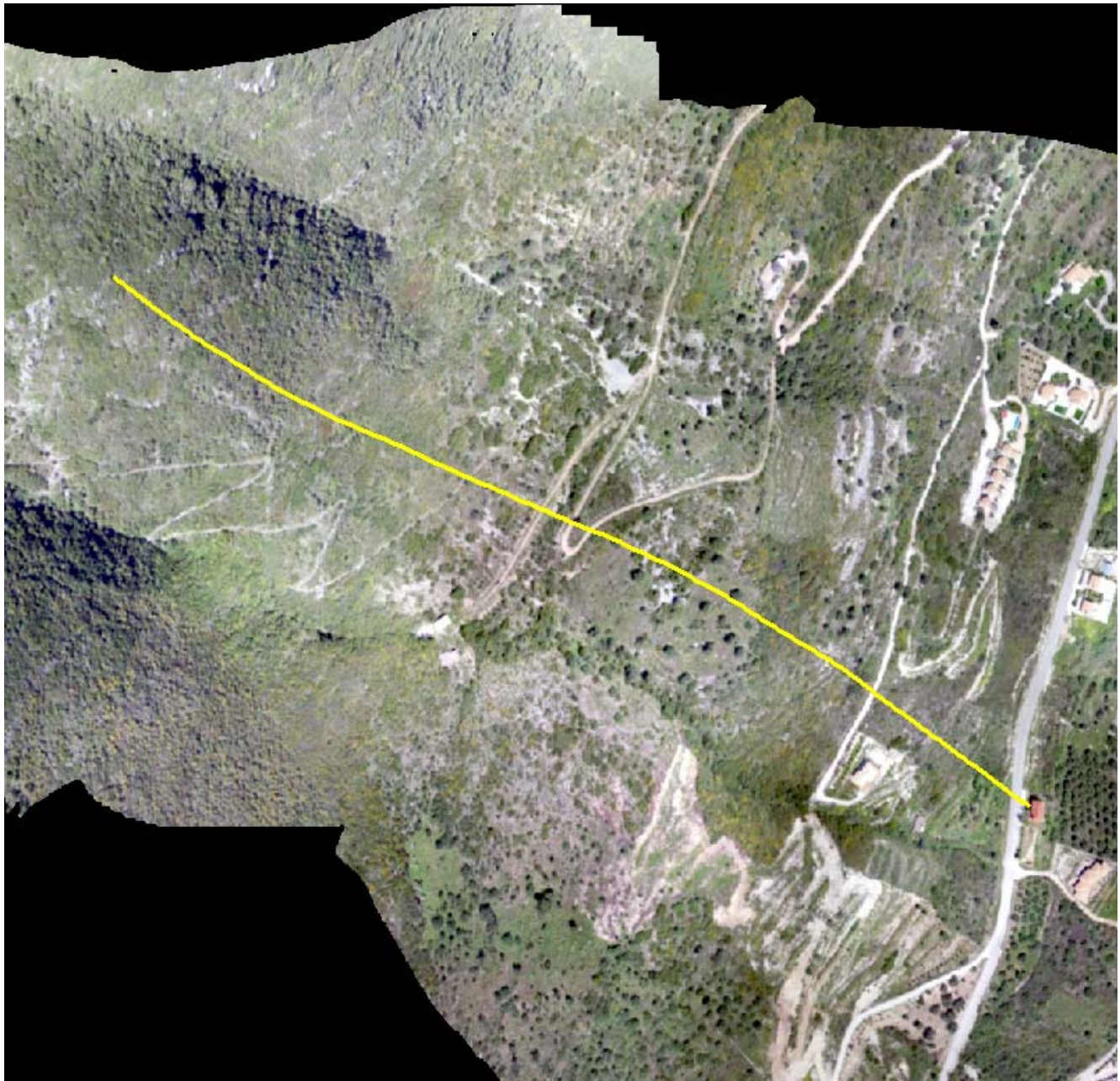
Figure 2. Orthophoto of case study. The total length of the trajectory shown with a yellow line, is 800 m.

Figure 3. Impact of rock on house in Ponti, Lefkada, Greece.
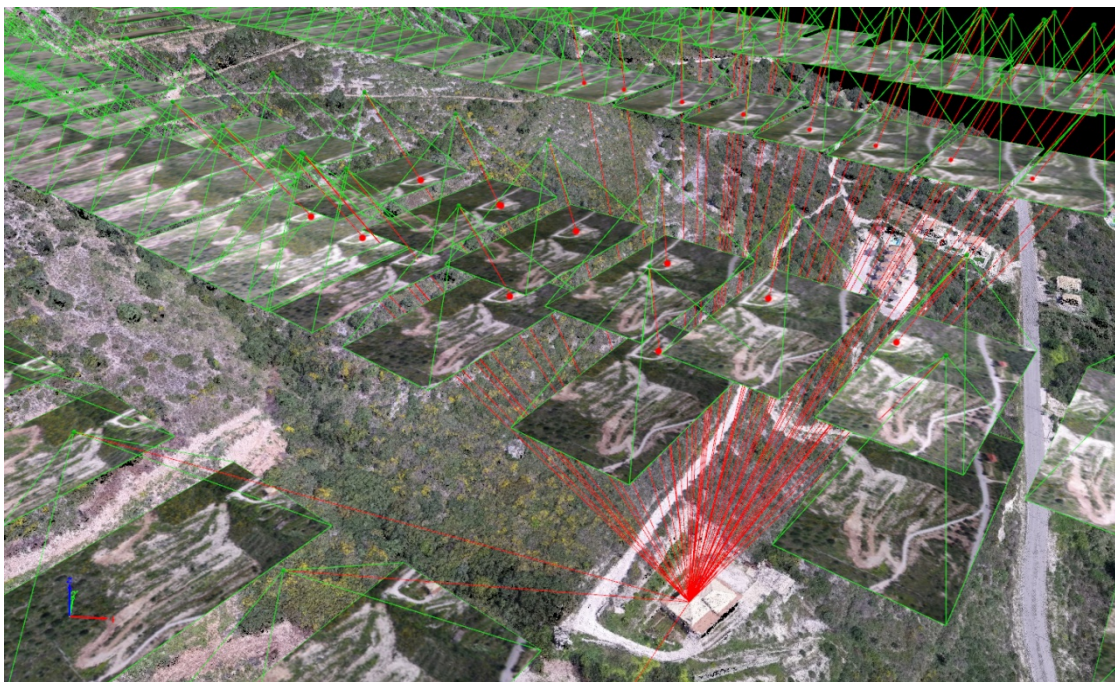
Figure 4. Schematic illustrating the overlap between pictures in the study site using SfM methodology.
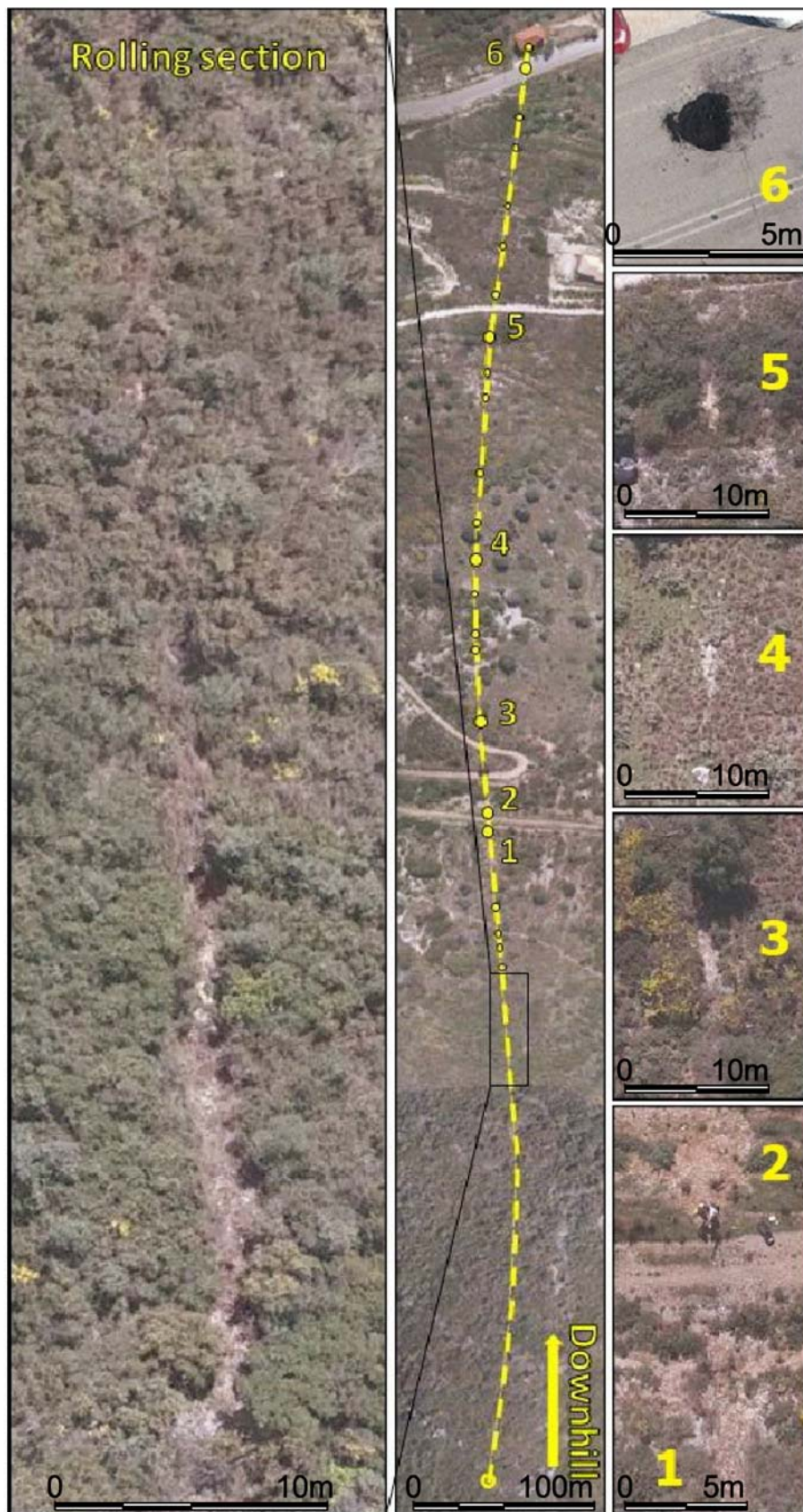
Figure 5. Top view orthophoto denoting rolling section, bouncing positions and indicative close-ups of impact points.
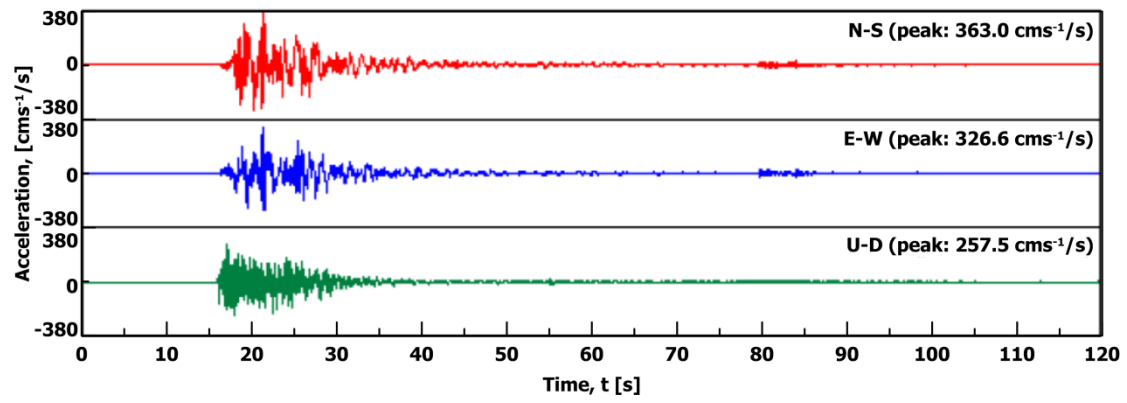
Figure 6. Acceleration time history recording at Vassiliki site (ITSAK, 2016)
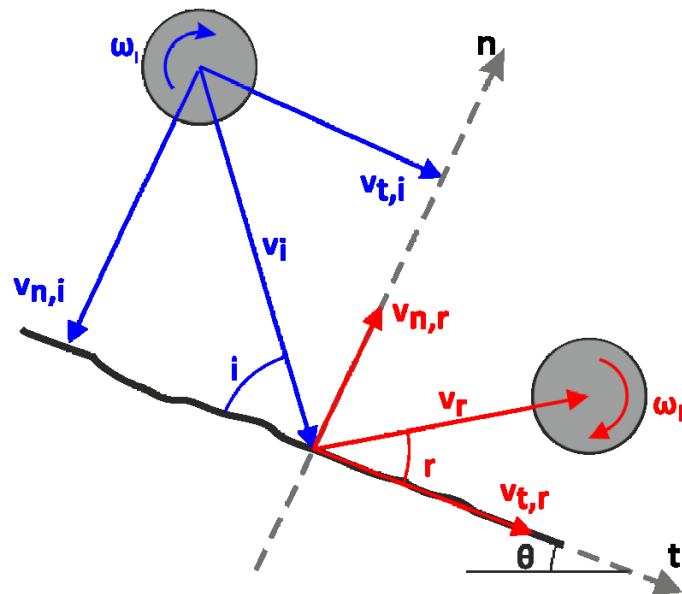
Figure 7. Coefficients of restitution
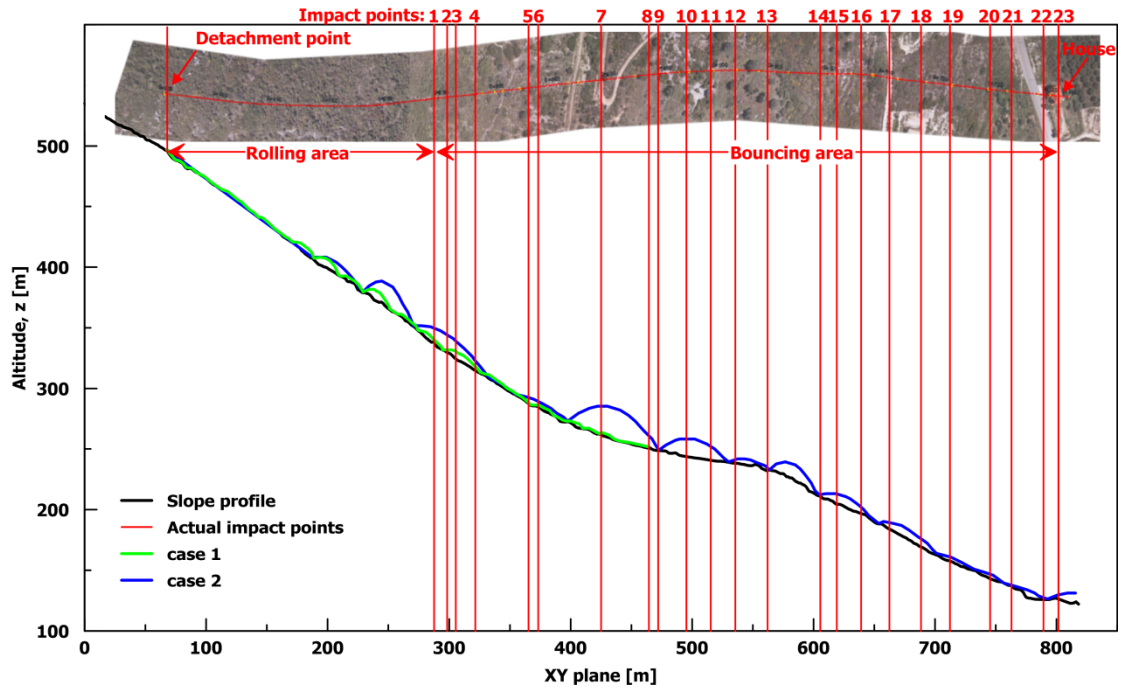
Figure 8. Plan view and cross section along block's path (units in m); 2D rockfall trajectory analysis results are plotted with green and blue line
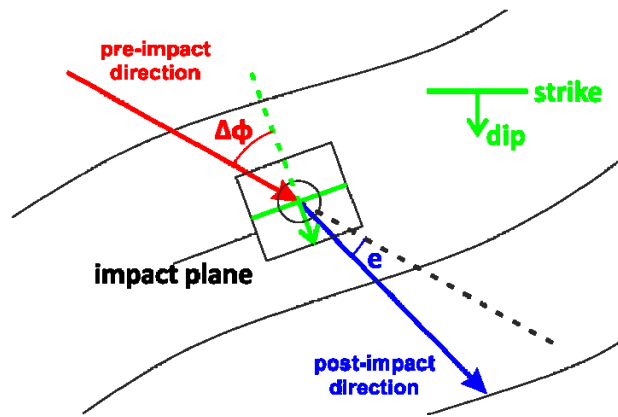
Figure 9 : Out of plane geometry
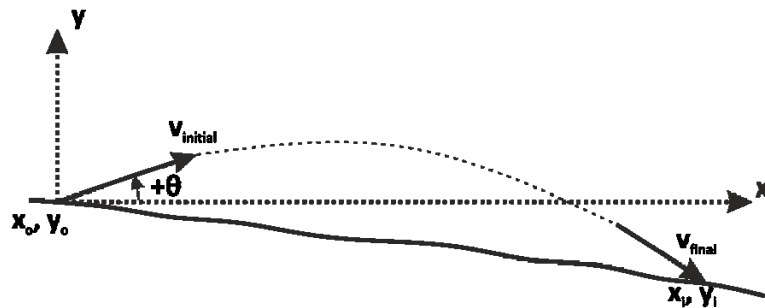
Figure 10. Parabolic segment
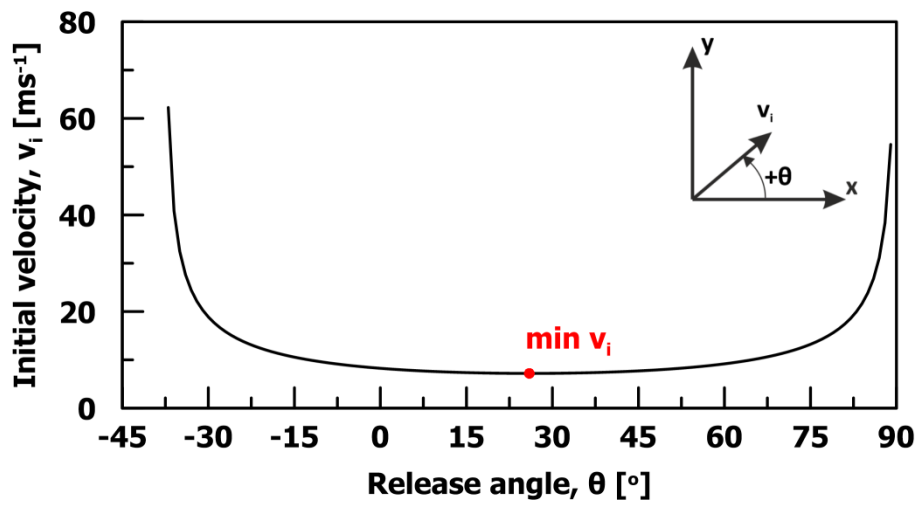
Figure 11. Release angle versus initial velocity for the first parabolic section (δx=10.75m, δy=8.33m)
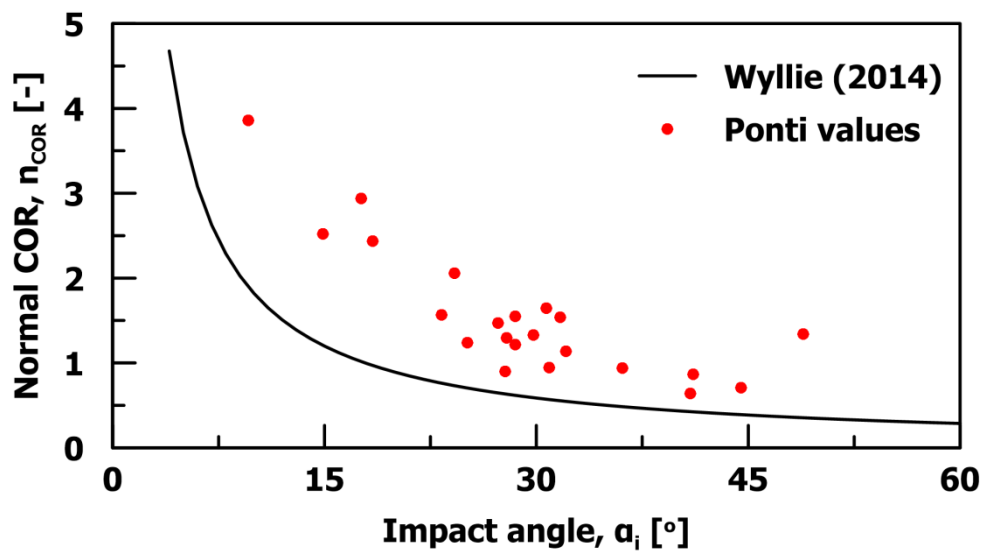
Figure 12. Normal COR versus impact angle
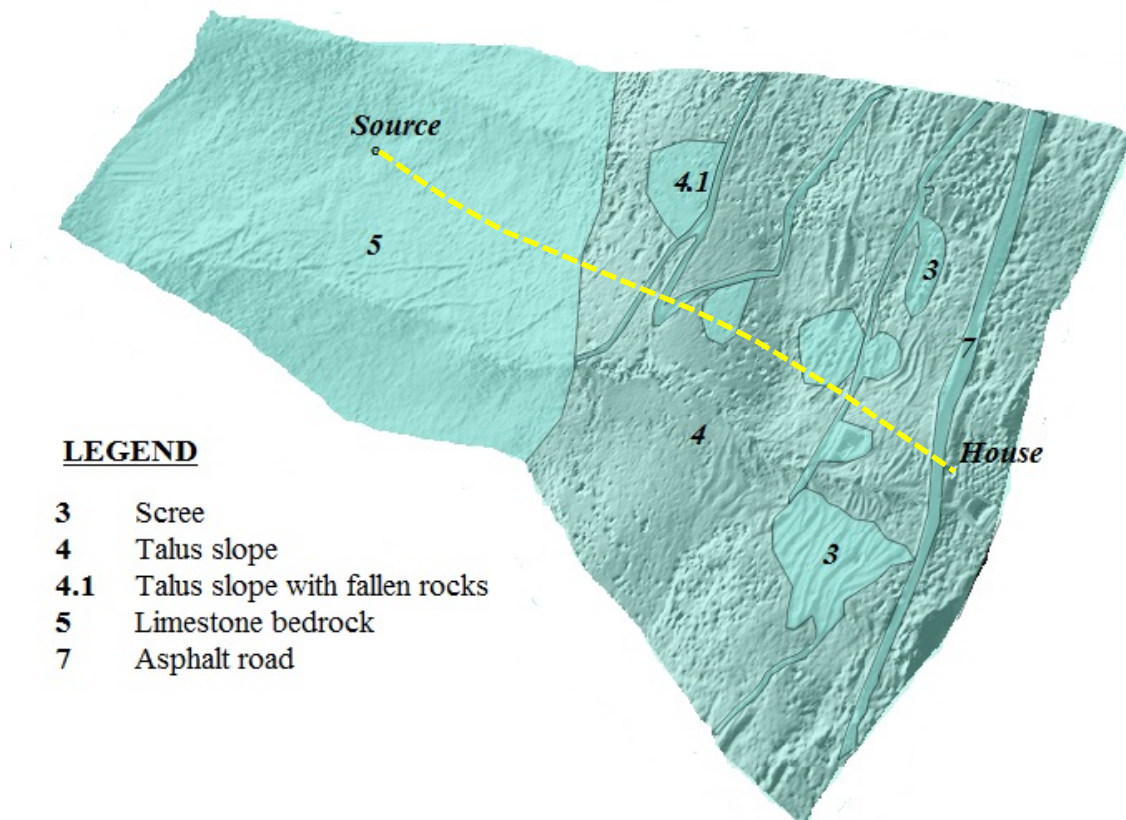
Figure 13. Soil types for 3D rockfall analysis (according to Rockyfor3D). Yellow path of trajectory is 800 m.
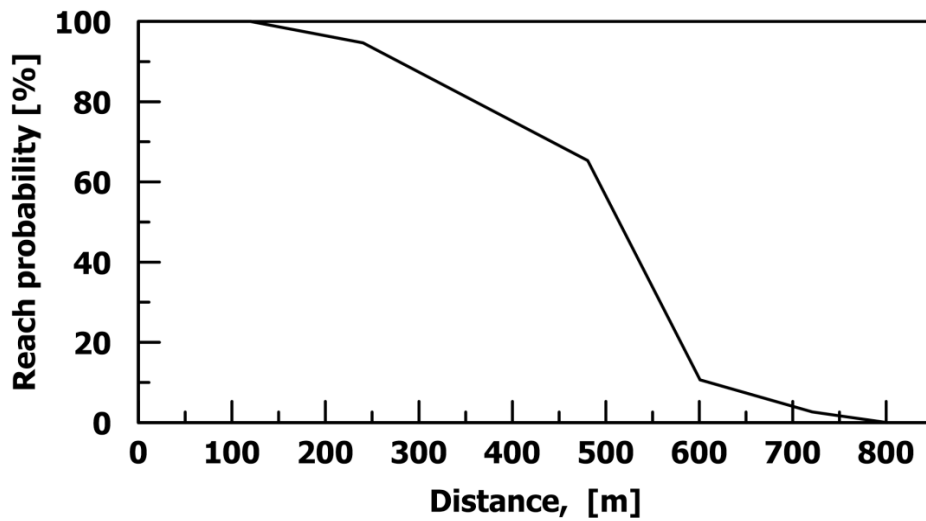
Figure 14. Reach probability graph calculated from 3D rockfall analysis
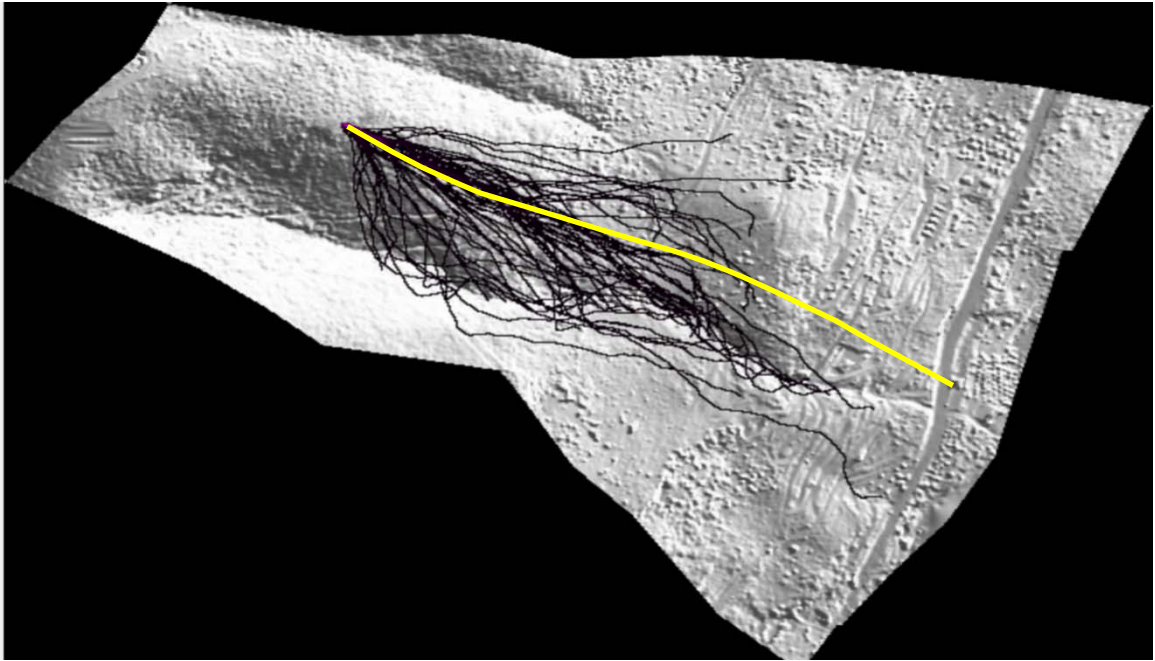
Figure 15. 3D trajectory analysis (from RockyFor3D analysis). Yellow line shows the actual trajectory. Black lines show the simulated trajectory.
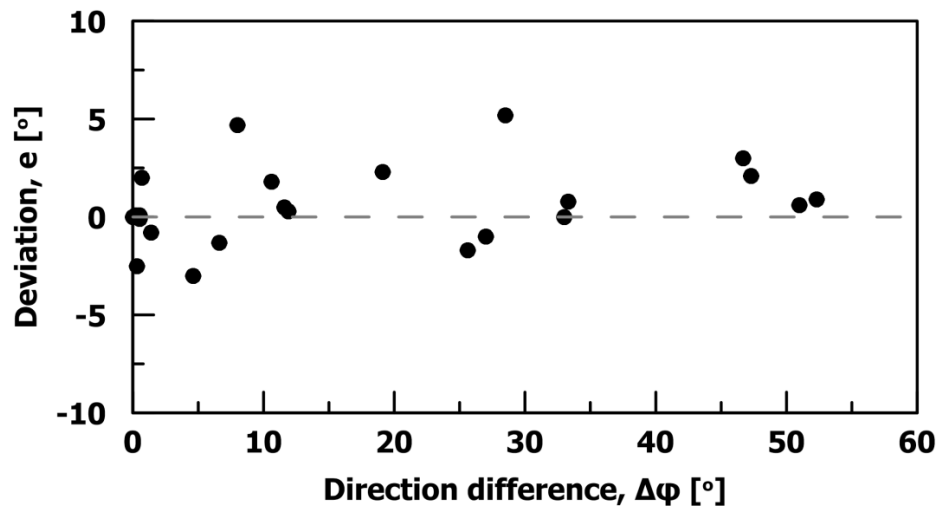
Figure 16. Deviation as a function of direction difference.